Electron-cloud alignment dynamics induced by an intense X-ray free-electron laser pulse: a case study on atomic argon

Check for updates

Laura Budewig[1,2], Sang-Kil Son[1] & Robin Santra [1,2] ✉

In an intense X-ray free-electron laser (XFEL) pulse, atoms are sequentially ionised by multiple X-ray photons. Photoionisation generally induces an alignment of the electron cloud of the produced atomic ion regarding its orbital-angular-momentum projections. However, how the alignment evolves during sequential X-ray multi-photon ionisation accompanied by decay processes has been unexplored. Here we present a theoretical prediction of the time evolution of the electron-cloud alignment of argon ions induced by XFEL pulses. To this end, we calculate state-resolved ionisation dynamics of atomic argon interacting with an intense linearly polarised X-ray pulse, which generates ions in a wide range of charge states with non-zero orbital- and spin-angular momenta. Employing time-resolved alignment parameters, we predict the existence of non-trivial alignment dynamics during intense XFEL pulses. This implies that even if initially the atomic electron cloud is perfectly spherically symmetric, X-ray multi-photon ionisation can lead to noticeable reshaping of the electron cloud.

Sequential multi-photon processes have attracted attention with the recent advent of X-ray free-electron lasers (XFELs)[1–5]. XFELs provide ultraintense and ultrashort X-ray pulses[6] with high degrees of typically linear polarisation[7,8]. Exposed to such an intense X-ray pulse, an atom absorbs more than one photon predominantly via sequences of one-photon ionisation events[9,10] accompanied by Auger-Meitner decay or X-ray fluorescence[11,12]. As a consequence of these so-called X-ray multi-photon ionisation dynamics[9], high atomic charge states are formed within a single X-ray pulse[10–15]. Because this unavoidably damages the electronic structure of the irradiated sample[16–20], applications of XFELs such as biomolecular imaging[21–29] are affected. Therefore, understanding X-ray multi-photon ionisation dynamics is critical. For atoms, they have been widely explored theoretically and/or experimentally based on ion[10–15,30–36], electron[12,35–37], and photon[12,14,33,36] spectra. Complementary information can be obtained by studying the electron cloud alignment of atomic ions, but this requires computationally expensive quantum state-resolved descriptions of atomic ions and X-ray-induced transitions[36,38,39].

An alignment of the electron cloud of atomic ions (hereinafter: ion alignment) with nonzero orbital-angular momentum is induced by photoionisation with different ionisation probabilities for different orbital-angular-momentum projection states[40–46]. As a consequence of this ion alignment, subsequently emitted Auger-Meitner electrons and fluorescence photons are anisotropically distributed[46–51] and fluorescence photons are also polarised[47,52,53]. Angular distributions of photoelectrons emitted from

the aligned ions are likewise affected[54] supplementary to their fundamental anisotropy[55–57]. On the one hand, all these make ion alignment experimentally accessible[42–44,51,53]. On the other hand, angle-resolved spectroscopy experiments[58–61] may profit from its theoretical study. However, how ion alignment is affected by X-ray multi-photon ionisation dynamics driven by an intense X-ray pulse is so far unknown.

Comparably strong alignments have been encountered in strong-field ionised[62,63] and resonantly-excited[64] atoms. Further, sequential double and triple ionisations driven by extreme ultraviolet (XUV) pulses have been investigated via photoelectron angular distributions[54,60,61,65,66]. Recently, alignment in XUV-ionised[39] and X-ray-ionised[38] atoms up to Kr^{3+}[39] and Ar^{3+}[38], respectively, has been theoretically explored with a focus on a single ionisation step. In all these studies, multiple competing sequences of photoionisation and accompanying decay processes were not systematically involved, either because they are absent or to simplify computations. But, they matter for the interaction with intense X-ray pulses.

Extending a former study[38], we here investigate the time evolution of ion alignment during an intense linearly polarised X-ray pulse. To this end, we performed state-resolved X-ray multi-photon ionisation dynamics calculations[36,38] for atomic argon (Ar), which simulate the time evolution of individual quantum-state populations. An individual quantum state is defined by an electronic configuration together with quantum numbers (L, S, M_L, κ). Here, L is the total orbital-angular momentum with projection M_L, S is the total spin-angular momentum (whose projection is irrelevant),

[1]Center for Free-Electron Laser Science CFEL, Deutsches Elektronen-Synchrotron DESY, Notkestr. 85, 22607 Hamburg, Germany. [2]Department of Physics, University of Hamburg, Notkestr. 9-11, 22607 Hamburg, Germany. ✉e-mail: robin.santra@cfel.de

and κ guarantees uniqueness. Individual quantum states differing only in M_L form an energy level, defined by an electronic configuration together with a term $^{2S+1}L(\kappa)$. Enabled by these calculations, not only time-resolved charge-state distributions and electron and photon spectra but also ion orbital- and spin-angular momentum and alignment are explored. We demonstrate that ion alignment (averaged over all individual quantum states populated at a given time) shows a highly non-linear behaviour and is suppressed by X-ray multi-photon ionisation dynamics. However, we find that the degree of alignment reached is not negligible for the individual atomic charge states populated.

Results

State-resolved X-ray multi-photon ionisation dynamics for Ar are calculated for an X-ray pulse having a temporal Gaussian pulse envelope of 10 fs FWHM (full width at half maximum) and a fluence (not volume-integrated) of 10^{12} photons per μm^2 (unless noted otherwise). These are typical XFEL pulse parameters[1,2,4], in particular for atomic, molecular, and optical physics instrumentations[67–70]. Such a high fluence has been realised not only in a series of gas-phase XFEL experiments on atoms, molecules, and clusters[10,13,31,37,71,72], but also in many serial crystallography experiments[27–29]. Even higher fluences are required for single-particle imaging at XFELs[16,19,20,29]. We consider X-rays being linearly polarised along the z axis

(quantisation axis) and intentionally chose Ar at a photon energy of 1.5 keV to increase the possibility of ion alignment induced by non-trivial ionisation dynamics. At this photon energy, there is no K-shell ($1s$) ionisation, which cannot create ion alignment without electron correlation effects[39]. Instead, L-shell ($2s$ and $2p$) photoionisation in Ar initiates non-trivial X-ray multi-photon multiple ionisation, including M-shell ($3s$ and $3p$) electrons. The target system can be any atomic species, including open-shell systems, when the above conditions are fulfilled. We chose neutral Ar atoms because corresponding gas-phase samples are straightforward to produce for experiments, and it is beneficial to have zero alignment at the beginning.

Ion, electron, and photon spectra

In order to examine the X-ray multi-photon ionisation dynamics of Ar driven by an intense linearly polarised X-ray pulse, we present in Fig. 1 calculated electron and photon spectra and charge-state distribution.

During the intense X-ray pulse, several photons per atom are absorbed sequentially. Consequently, a wealth of spectral lines characterises the time-resolved photoelectron spectrum in Fig. 1a. Here, the vertical and horizontal axes are the time and energy, using 0.4-fs and 1-eV bins, respectively. The photoelectron spectrum is grouped into large L-shell and minor M-shell spectra. Each subspectrum is dominated by lines for the ionisation of neutral Ar, occurring early in time. These lines are followed in time by a flat quasi-
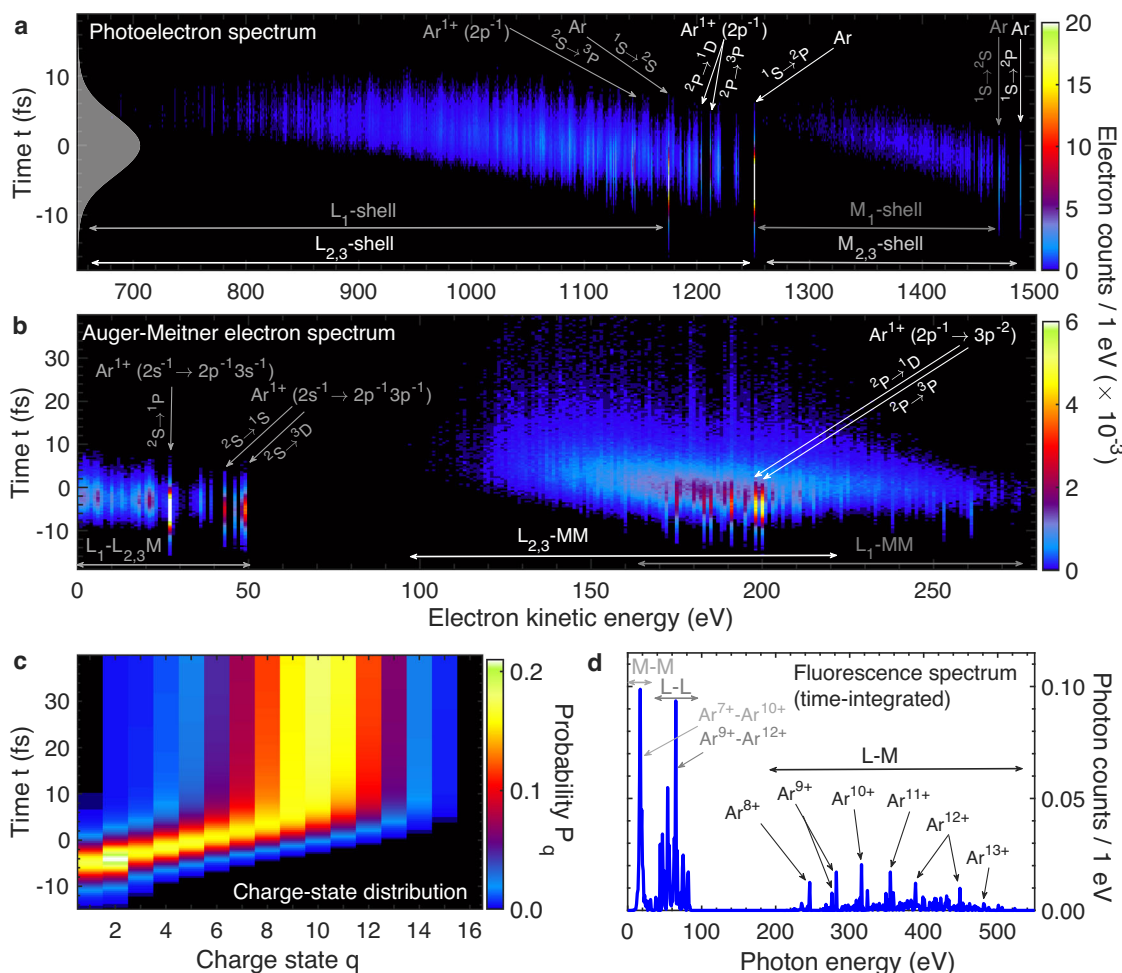
Fig. 1 | Overview of X-ray multi-photon ionisation dynamics of Ar at a photon energy of 1.5 keV, a fixed fluence of 10^{12} photons per μm^2, and a pulse duration of 10 fs FWHM. a Time-resolved photoelectron spectrum. The temporal shape of the X-ray pulse is depicted with a grey-shaded area. **b** Time-resolved Auger-Meitner electron spectrum. **c** Time evolution of the charge-state distribution. **d** Time-integrated fluorescence spectrum. In panels **a**, **b**, and **d**, double arrows indicate the subspectra, defined by the involved subshells, i.e., L_1 ($2s$), $L_{2,3}$ ($2p$), M_1 ($3s$), and/or $M_{2,3}$ ($3p$). In **b** and **d**, the first subshell index refers to the initial vacancy, whereas the latter refer to the subshells from which the electrons are removed. Single arrows indicate ions involved in the transition via initial charge state, involved electronic configuration(s) (holes indicated), and/or terms (^{2S+1}L). For all panels, the statistical errors obtained via bootstrap estimate are too small to be shown.
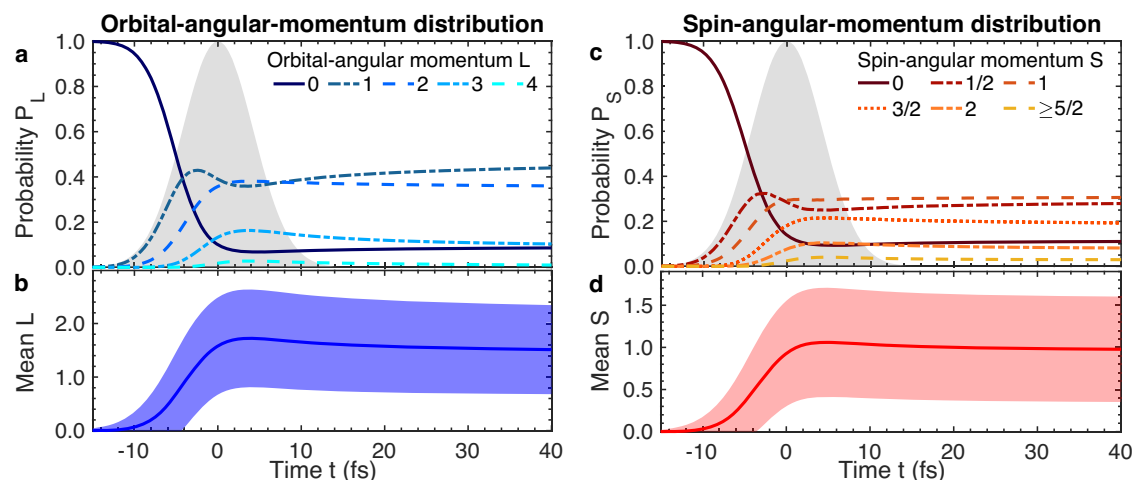
Fig. 2 | Time evolution of ion orbital-angular momentum L and spin-angular momentum S of Ar induced by an intense XFEL pulse with a fixed fluence of 10^{12} photons per μm^2. a Probability P_L of individual L. **b** Mean of the orbital-angular-momentum distribution together with its width (area around mean). **c, d** The spin-angular-momentum distribution is presented likewise (with $S = 5/2, \dots, 4$ collected in one line). The temporal pulse shape is depicted by the grey-shaded areas in **a** and **c**. For all panels, the statistical errors obtained via bootstrap estimate are too small to be shown.

continuum, moving toward lower energy and weaker lines with time. The quasi-continua are generated by photoionisation of ions produced by preceding ionisation and/or decay processes. These intermediate ions, generally, exhibit a manifold of relatively weak state-to-state transitions between different energy levels.

L-shell ionisation is mostly immediately accompanied by Auger-Meitner decay as demonstrated by the time-resolved Auger-Meitner electron spectrum in Fig. 1b. Similar to the photoelectron spectrum, the Auger-Meitner electron spectrum exhibits two energetically-separated quasi-continua, the *L–LM* and *L–MM* spectra. Here, an Auger-Meitner channel *L–MM* means that an initial *L*-shell vacancy is filled by an electron from the *M*-shell, accompanied by the ejection of another electron from the *M*-shell. In the *L–LM* channel the initial *L*-shell vacancy decays such that in the final state, one electron has been removed from a higher-lying *L*-shell orbital and the other electron has been removed from the *M*-shell. The *L–LM* and *L–MM* spectra are generated by a plethora of energy levels involved in the given channels. The *L–LM* spectrum dominates at early times up to around 5 fs, but is energetically forbidden later. In contrast to the *L–LM* spectrum, the *L–MM* spectrum extends to times beyond the X-ray pulse due to the long lifetimes of some intermediate ion states. Nonetheless, most Auger-Meitner decays ($\approx 95\%$) take place within 40 fs after the peak of the X-ray pulse.

As a result of sequences of one-photon ionisation accompanied by Auger-Meitner decay, charged ions are formed as shown by the time-resolved charge-state distribution in Fig. 1c. Here, the sum of probabilities P_q of all charge states q ($q = 0, +1, \dots, +16$) is unity at each time. As can be seen, charged ions are formed sequentially as time goes by, with most changes before and around the peak of the X-ray pulse. When the X-ray pulse is over, most ions ($\approx 78\%$ at 40 fs) have reached a charge of $+8$ to $+12$.

The highly-charged ions relax via fluorescence into stable states when the X-ray pulse is over and Auger-Meitner decay is suppressed by a lack of *M*-shell electrons. This is depicted in Fig. 1d by the time-integrated fluorescence spectrum, generated by Ar^{7+} to Ar^{13+}. Fluorescence is a very weak process, especially without *K*-shell holes. The associated lifetimes range from 674 fs (Ar^{15+} $1s^2 2s^0 2p^0 3s^0 3p^1$) to 8×10^5 fs ($Ar^{15+} 1s^2 2s^0 2p^1 3s^0 3p^0$) (state-resolved fluorescence rate calculations[38]). Therefore, fluorescence predominantly occurs for highly-charged ions after the end of the X-ray multi-photon ionisation dynamics. Only about 1% of fluorescence decays take place within 40 fs after the peak of the X-ray pulse.

Orbital- and spin-angular-momentum distributions
The time-resolved orbital-angular-momentum distribution is of interest because alignment parameters consider ions with definite orbital-angular

Table 1 | Orbital- and spin-angular-momentum distributions when the pulse is over and all decay processes are completed

| L	0	1	2	3	4	
$P_L(t \to \infty)$	0.23	0.60	0.17	0.00	0.00	
S	0	1/2	1	3/2	2	$\geq 5/2$
$P_S(t \to \infty)$	0.12	0.30	0.30	0.17	0.07	0.04

The corresponding time evolution is shown in Fig. 2.

momentum L. In Fig. 2a, we plot the time-resolved probability P_L of ions with definite L ($L = 0, \dots, 4$), which is given by all individual quantum states with quantum number L populated at a given time. Initially, neutral Ar is in an S-state ($L = 0$) and is included in $P_{L=0}$. Induced by the X-ray pulse, neutral Ar turns into ions in P-states ($L = 1$; up to $\approx 43\%$). In subsequent sequences of one-photon ionisation accompanied by Auger-Meitner decay, also D-states ($L = 2$; up to 38%), a few F-states ($L = 3$; $< 16\%$), and little G-states ($L = 4$; $< 3\%$) are formed at the expense of S- and P-states. F- and G-states are rare because unstable electronic configurations with several holes simultaneously in the $2p$- and $3p$-shells are required. As a consequence of their instability, they (stepwise) decay into stable S- and P-states. Note that these decays occur on time scales much longer than the time window in Fig. 2a. In the end (when all decay processes are completed) many P-states, some S- and D-states, but neither F- nor G-states are left over (Table 1). In Fig. 2b, the mean of the orbital-angular-momentum distribution $\bar{L} = \sum_L L P_L$ and its width $\Delta_L = \sqrt{\sum_L L^2 P_L - \bar{L}^2}$ are shown. The maximum mean and width are reached shortly after the peak of the X-ray pulse (at about 4 fs), which stresses that at this time the maximum number of ions with $L > 1$ is achieved.

The time-resolved spin-angular-momentum distribution, shown in Fig. 2c, d, scrutinises the spin S ($S = 0, 1/2, \dots, 4$) instead of L. Similar to the orbital-angular-momentum distribution, the majority of ions is found in low non-zero spin states ($S = 1/2, 1, 3/2$) during and after the X-ray pulse. The maximum mean spin is also reached shortly after the peak of the X-ray pulse. The difference is that the spin-angular-momentum distribution barely evolves after the X-ray pulse is over (compare Fig. 2c and Table 1). This is because Auger-Meitner and fluorescence decays change S only by 1/2 or not at all, respectively (non-relativistic selection rules). Consequently, decays from some very high spin states, generally having low L, are spin-forbidden.

Ion alignment dynamics
Before defining the time-dependent alignment parameter, let us explore in Fig. 3a–d the time-resolved distribution of orbital-angular-momentum
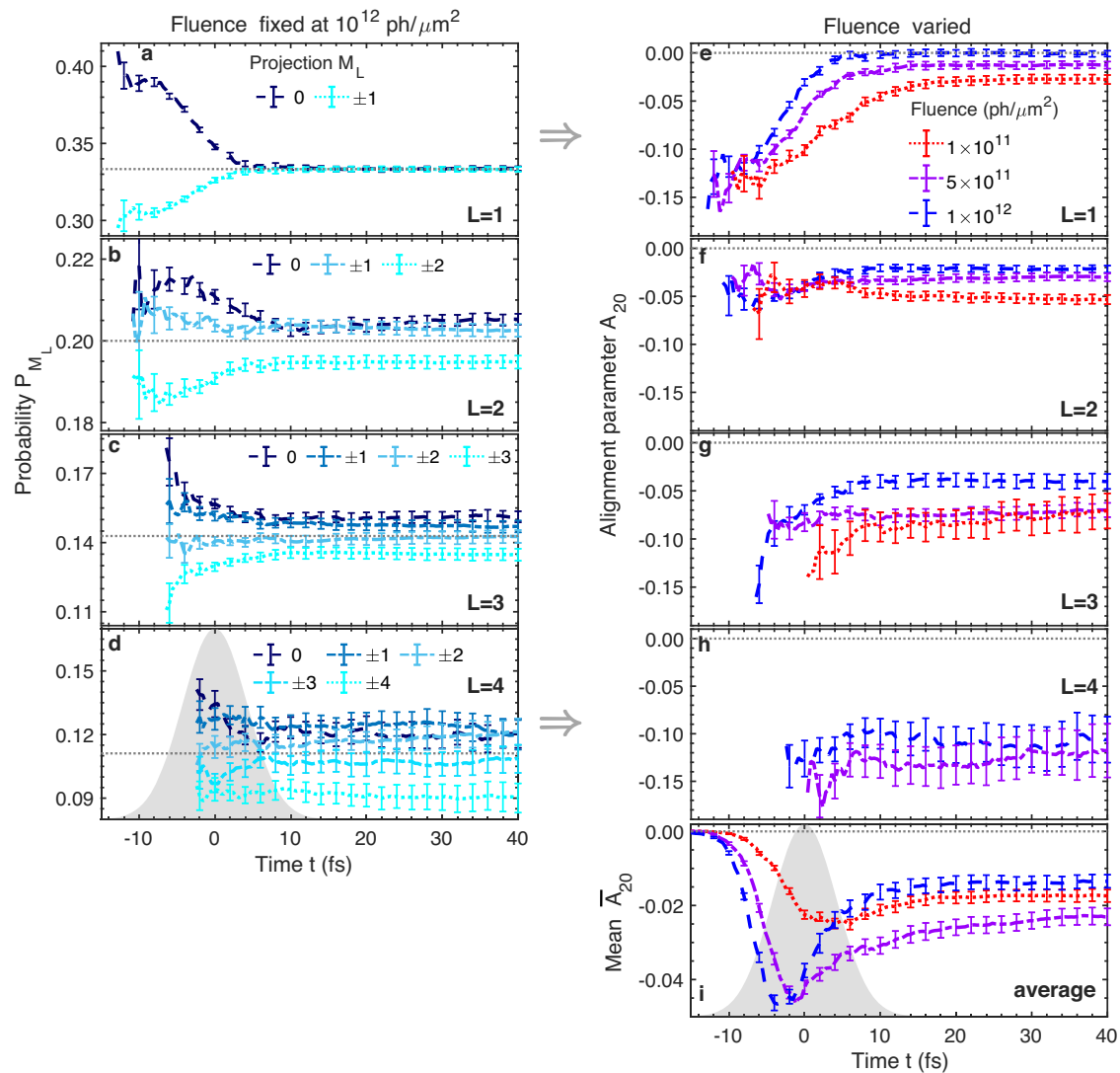
Fig. 3 | Alignment dynamics of Ar ions induced by an intense XFEL pulse.
a–d The distribution of orbital-angular-momentum projections M_L of ions with definite orbital-angular momentum L is shown by their probabilities P_{M_L} as a function of time at a fixed fluence of 10^{12} photons per μm^2. The dotted grey lines at $1/(2L+1)$ indicate a uniform distribution. **e–h** From the probabilities P_{M_L} the alignment parameter A_{20} for a definite L is calculated and compared for three different fluences. **i** The mean alignment parameter $\bar{A}_{20}$, averaged over all L, is shown for the same fluences. In all panels, the error bars every 2 fs indicate the statistical error obtained via bootstrap estimate. Insufficient statistics are avoided by the restriction $P_L \geq 0.005$ at each time step (**a–h**). The temporal pulse shape is sketched by grey shading in **d** and **i**.

projections M_L for the given L. For ions with definite L, the probabilities P_{M_L} of $M_L = -L, \ldots, +L$ are obtained by summing up probabilities of all individual quantum states with M_L for the given L and at a given time. Note that $P_{M_L} = P_{-M_L}$ because no orientation[38,45] is created by linearly polarised X-rays. For the dominating P-state ($L = 1$), we observe in Fig. 3a that at the beginning of the X-ray pulse and the X-ray multi-photon ionisation dynamics, P-states are aligned along the X-ray polarisation direction ($P_{M_L=0} > P_{M_L=\pm1}$). In the course of X-ray multi-photon ionisation dynamics, their alignment is reduced ($P_{M_L=0}$ decreases, whereas $P_{M_L=\pm1}$ increases), until an almost uniform distribution ($P_{M_L=0} = P_{M_L=\pm1} = 1/3$) is reached shortly after the peak of the X-ray pulse (at about 3 fs). For higher L (Fig. 3b–d), no uniform distribution (the dashed line) is reached after the X-ray pulse and, consequently, their alignment is less reduced (which is further discussed later). The statistical errors are larger than those for $L = 1$ due to smaller numbers of realisations.

The degree and direction of alignment is described by the alignment parameter A_{20}, which is also applicable to ion ensembles. Based on the

probabilities P_{M_L}, A_{20} for ions with definite L is defined as[38,45,73,74]

$$A_{20}(L) = \sqrt{\frac{5}{f_L}} \times \sum_{M_L} \left[3M_L^2 - L(L+1) \right] P_{M_L}, \qquad (1)$$

where $f_L = (2L+3)(L+1)L(2L-1)$. The alignment parameter is negative ($A_{20} < 0$), when ions with smaller $|M_L|$ are more populated than others, and positive ($A_{20} > 0$), when ions with larger $|M_L|$ are more populated. $A_{20} = 0$ indicates a uniform distribution. The meaning of A_{20} is further elaborated on in the next section, and extreme values of A_{20} are listed in Table 2. The A_{20} calculated with the time-resolved probabilities P_{M_L} in Fig. 3a–d is shown for the given L in Fig. 3e–h (blue line for a fixed fluence of 10^{12} photons per μm^2). For P-states, A_{20} is initially about -0.16, which is already not an extremely strong alignment compared to the perfect alignment of $A_{20} = -\sqrt{2}$ (Table 2). With time $|A_{20}|$ decreases almost to zero. For higher L, A_{20} is also negative, but with only a weakly declining trend in time.

Table 2 | Perfect alignment ($A_{20} < 0$) and anti-alignment ($A_{20} > 0$) where all ions have either $M_L = 0$ or $M_L = |L|$, respectively
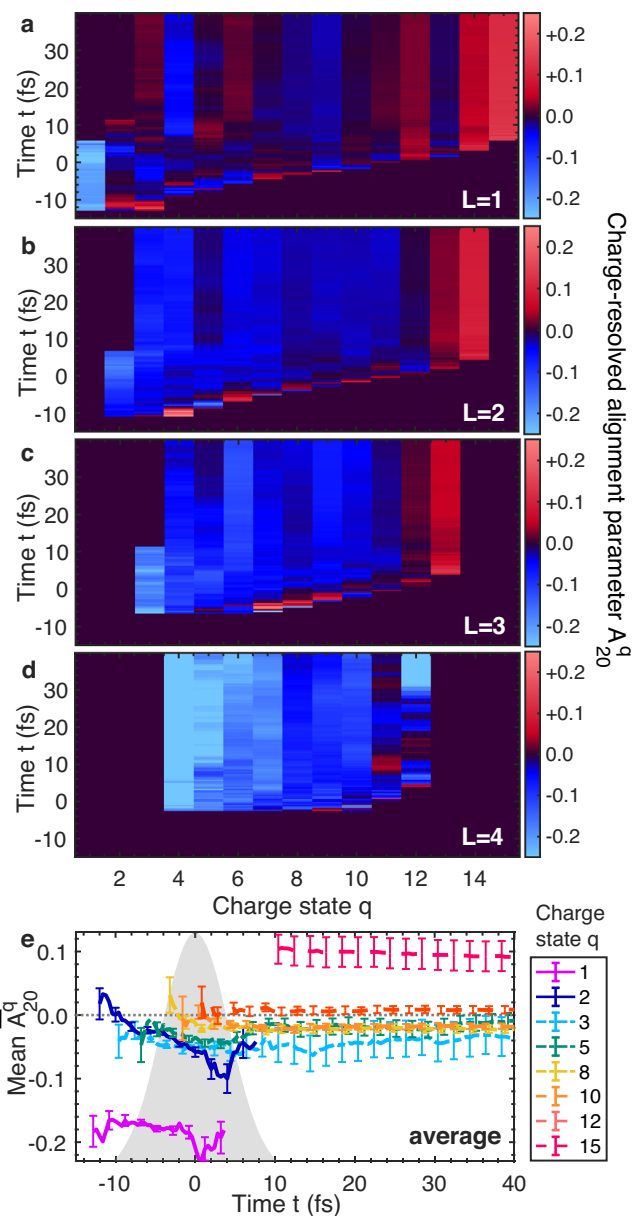
	Alignment parameter A_{20}	
L	$M_L = 0$	$M_L = |L|$
1	$-\sqrt{2}$	$\sqrt{1/2}$
2	$-\sqrt{10/7}$	$\sqrt{10/7}$
3	$-\sqrt{4/3}$	$\sqrt{25/12}$
4	$-\sqrt{100/77}$	$\sqrt{28/11}$

This gives the minimum or the maximum alignment parameter A_{20}.

Figures 3 e–h also show how the alignment of each L depends on the X-ray fluence applied (number of incoming X-rays per unit area[9]). Fluence-dependencies are important in volume integration[75], necessary for quantitative comparisons with experiments. The fluence of 10^{12} photons per μm^2, considered so far, is compared with two lower fluences: 5×10^{11} photons per μm^2 and 10^{11} photons per μm^2. No strong fluence-dependence of A_{20} is observed because ionisation dynamics are mainly only reduced and delayed with lower fluence. For lower fluences, therefore, the evolution of A_{20} is delayed, so that the alignment is less reduced with time. Thus, the saturation value reached after the X-ray pulse is sensitive to the X-ray fluence applied, and its absolute magnitude decreases as the fluence increases. We observe that the absolute magnitude of this saturation value is enhanced with increasing L, which is to be further analysed later. As a result, for $L > 1$, alignment is not negligible for all fluences, in contrast to P-states.

Figure 3i demonstrates what happens to the ion alignment when averaging over L. It shows the mean alignment parameter $\bar{A}_{20} = \sum_L P_L \times A_{20}(L)$ (unaligned neutral Ar included). As can be seen, $\bar{A}_{20}$ exhibits a highly non-linear behaviour. Before the X-ray pulse, neutral Ar is unaligned ($\bar{A}_{20} = 0$). At the beginning of the X-ray pulse, p-shell ionisation of neutral Ar creates a negative ion alignment ($\bar{A}_{20} < 0$) and $|\bar{A}_{20}|$ increases as more ions are produced. Around the peak of the X-ray pulse, $|\bar{A}_{20}|$ is maximised ($\bar{A}_{20} \approx -0.047$ for 10^{12} photons per μm^2). At this time, most neutral Ar is already ionised (see $P_{q=1}$ in Fig. 1c). If there were only single photoionisation, $|\bar{A}_{20}|$ would continue increasing up to $\bar{A}_{20} \approx -0.12$ (ensemble of Ar^{1+} produced in 59% by p-shell ionisation). However, due to progressing photoionisation accompanied by Auger-Meitner decay involving mainly P- and D-states, $|\bar{A}_{20}|$ noticeably decreases. A saturation value is reached at the end of the X-ray pulse, which is clearly sensitive to the X-ray fluence applied. On the one hand, the higher the fluence, the more $|\bar{A}_{20}|$ is reduced compared to its maximum because of enhanced X-ray multi-photon ionisation dynamics. On the other hand, for low fluence (10^{11} photons per μm^2), only around 50% of the atoms are ionised at all and, thus, the maximum of $|\bar{A}_{20}|$ is very small. As a consequence, to see a maximum alignment, the fluence should be large enough to ionise most atoms ($> 10^{11}$ photons per μm^2), but should not induce too much X-ray multi-photon ionisation dynamics ($< 10^{12}$ photons per μm^2).

To analyse the ion alignment further, we present in Fig. 4a–d charge-resolved alignment parameters A_{20}^q for different L. Note that $A_{20}(L) = \sum_{q=1}^{16} P_q^L A_{20}^q(L)$ with the charge-state probabilities P_q^L for definite L ($\sum_{q=1}^{16} P_q^L = 1$). P_q^L evolves sequentially in time and charge similar to P_q (Fig. 1c) though lack of initially neutral Ar causes much larger P_q^L for low q at early times. A_{20}^q is clearly non-zero and exhibits very different values and signs for different q and L. For P-states, intermediately-charged ions are weakly aligned ($A_{20}^q < 0$) or weakly anti-aligned ($A_{20}^q > 0$) along the X-ray polarisation (Fig. 4a). But Ar^{1+} produced early by single $2p$ or $3p$ ionisation[38] is clearly aligned along the X-ray polarisation ($A_{20}^{q=1} \approx -0.21$) and Ar^{14+} and Ar^{15+} produced less and later are clearly anti-aligned ($A_{20}^{q=14} \approx +0.05$). For P-states, only $P_{M_L=0}$ and $P_{M_L=\pm1}$ determined the A_{20} value. $P_{M_L=0} > P_{M_L=\pm1}$ results in a negative A_{20}, while $P_{M_L=0} < P_{M_L=\pm1}$ gives a positive A_{20}. Typically, p-shell ionisation preferentially increases $P_{M_L=0}$[38].

Fig. 4 | Differently charged Ar ions demonstrate different degrees and directions of alignment. a–d The charge-resolved alignment parameter A_{20}^q for different orbital-angular momenta L. Red and blue indicate $A_{20}^q > 0$ and $A_{20}^q < 0$, respectively. **e** The average over all L for selected charge states q. Grey shading indicates the temporal pulse shape. Error bars obtained via bootstrap estimate are shown only in **e**. In **a–d**, they are not shown, but are slightly larger than those in **e**. Insufficient statistics are avoided by the restriction $P_q^L \geq 0.005$ at each time step. A fluence of 10^{12} photons per μm^2 is used.

On the other hand, the $M_L = 0 \rightarrow M_L = 0$ transition is prohibited when the sum of ion and involved bound electron angular momenta is odd, which effectively increases $P_{M_L=\pm1}$. The interplay of these two tendencies combined with the manifold of parallel and competing state-to-state transitions reduces the degree of alignment and changes its direction, already for Ar^{2+}. For comparison, a single (unaveraged) sequence of $2p$ ionisation and Auger-Meitner decay leads to $A_{20}^{q=2} \approx 0.1$[38]. In contrast to P-states, $|A_{20}^q|$ for $L > 1$ is larger and becomes clearly positive only for very highly charged ions ($q \geq 12$). This is attributed to a reduced effect of prohibited transitions on the alignment when the ions involved in a transition have higher L. It also explains why in Fig. 3 a non-vanishing alignment is observed for $L > 1$ at
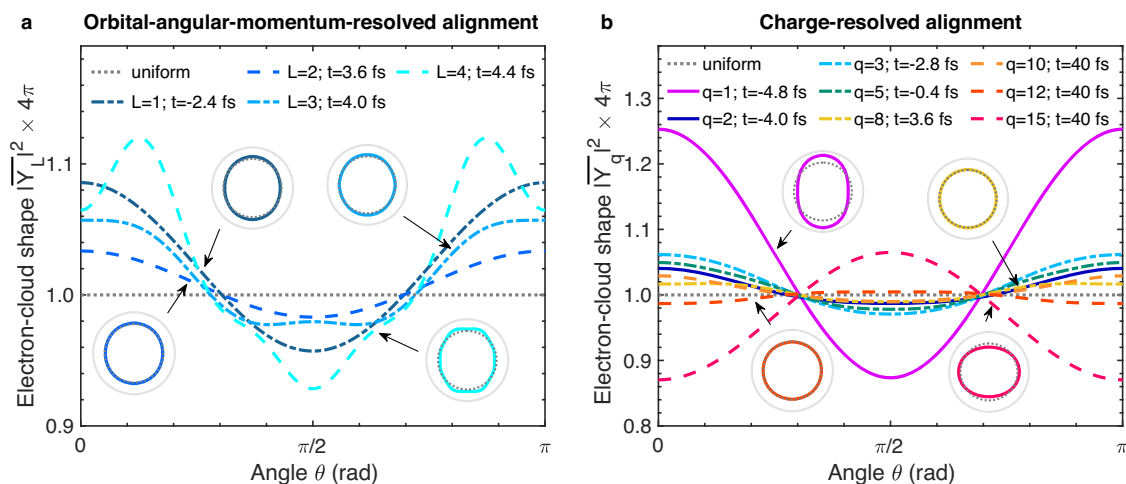
Fig. 5 | Spatial shape of the electron cloud of Ar ions produced by an intense XFEL pulse at specific points t in time. a Electron-cloud shape $|\bar{Y}_L|^2$ for ions with definite orbital-angular momentum L (charge-averaged) at time t with maximum P_L (Fig. 2a). **b** Electron-cloud shape $|\bar{Y}_q|^2$ for ions in a few selected charge states q (L-averaged) at time t with maximum P_q (Fig. 1c). The insets in both panels show polar plots of a few selected electron-cloud shapes. The vertical axis ($\theta = 0$ rad and $\theta = \pi$ rad) corresponds to the X-ray polarisation axis. A fluence of 10^{12} photons per μm² is used.

long times in contrast to $L = 1$. In Fig. 4e, the charge-resolved alignment parameter $\bar{A}_{20}^q$ averaged over all L is presented for selected q. From Figs. 3i and 4e, we conclude that the reduction of ion alignment is mostly the result of averaging over all L and q. Our results suggest that L-resolved or q-resolved quantities are beneficial for detecting ion alignment dynamics.

Spatial shapes of aligned electron clouds

To develop some intuition about ion alignment, we show in Fig. 5 spatial shapes of electron clouds for selected ions produced at some exemplary times t. At the times selected, the corresponding ion yield becomes the largest during the time evolution; the corresponding alignment parameters as a function of time are given in Figs. 3 and 4. In Fig. 5a, we consider ions with different L, but average over all q. The spatial shape of the electron cloud, averaged over all projections M_L, is determined by using the quantity

$$|\bar{Y}_L(\theta)|^2 = \sum_{M_L=-L}^{L} P_{M_L} |Y_L^{M_L}(\theta,\phi)|^2. \quad (2)$$

Here, $Y_L^{M_L}$ is a spherical harmonic (squaring eliminates the ϕ-dependence) and P_{M_L} is the time-resolved probability for definite L at time t (Fig. 3a–d). In Fig. 5b, we consider ions in a few selected charge states q, but average over all L. In this case, the spatial shape of the electron cloud, $|\bar{Y}_q(\theta)|^2$, is the L-average over all $|\bar{Y}_L(\theta)|^2$ [Eq. (2)] after replacing the P_{M_L} with the $P_{M_L}^q$ underlying A_{20}^q (Fig. 4). Taking the vertical axis as the X-ray polarisation (z) axis, we observe for most selected electron clouds an oval, prolate shape (corresponding to $A_{20} < 0$). Only highly-charged ions ($q \geq 12$) exhibit an oblate shape ($A_{20} > 0$). For a few selected electron clouds ($L = 4$ in Fig. 5a and $q = 1, 15$ in Fig. 5b) the deviations from a uniform distribution (circle; dotted grey lines in Fig. 5) are quite pronounced and clearly visible in the polar plots.

Discussion

The present paper presents a complete state-resolved description of X-ray multi-photon ionisation dynamics, including electron-cloud alignment in an XFEL pulse. The calculated alignment parameter for Ar^{1+} ($A_{20}^{q=1} \approx -0.21$) acceptably agrees with previous works[38,44,54], taking into account the photon-energy dependence. Due to X-ray multi-photon ionisation, the magnitude of the alignment parameter after averaging over L and q becomes relatively small (< 0.05) as depicted in Fig. 3i. However, when we analyse the alignment parameter for individual L and q (Fig. 4a–d),

individual L (Fig. 3e–h), and individual q (Fig. 4e), its magnitude is larger than the averaged value. Non-trivial ion alignment dynamics for individual quantum states are predicted. We expect that this result can be generalised to other atomic species (ionised under suitable conditions), photon energies (below the respective K-shell threshold), and (femtosecond) pulse durations. Observing electron-cloud alignment dynamics induced by XFEL pulses requires few-femtosecond- or even attosecond-resolved measurements sensitive to M_L quantum-state distributions.

Desirable are time-resolved measurements of Auger-Meitner electron angular distributions[42,44,48,49,76] generated in XFEL experiments. Best suited for this propose are transitions involving only a single continuum wave for the Auger-Meitner electron[48,49], e.g., final ions with zero L. Then, the anisotropy parameter[47,50,77–80] is directly proportional to the alignment parameter for the initial ion. Future developments in this direction will enable deeper insights into electron-cloud alignment in an XFEL pulse, including the impact of effects so far neglected, such as non-dipole effects[54,66,81] or spin-orbit coupling[62–64,82]. A further possibility is to apply circularly polarised X-ray pulses[8,83–86]. Even though the direction of alignment changes[40], based on the present results, we expect similar electron-cloud alignment dynamics during a circularly polarised X-ray pulse. However, how the orientation induced by the circularly polarised X-ray pulse behaves is an open question.

Lastly, we would like to comment on electric alignment (orientation) in molecular targets induced by XFEL pulses. Here, we demonstrate that the polarisation of the X-ray beam is imprinted on the atomic electron-cloud dynamics on ultrafast time scales. We anticipate a similar impact on the electron-cloud dynamics in molecules. However, this depends in detail on the strength of interatomic interactions and remains to be investigated in a future study.

Methods

For X-ray multi-photon ionisation dynamics calculations, we employ XATOM[20,87,88], which has been successfully applied for interpreting XFEL experiments[11–15,31,32,34,35,89]. XATOM has recently been extended to state-resolved ionisation dynamics with a Monte Carlo implementation[36], based on a non-relativistic quantum-state-resolved electronic-structure framework[38] for isolated atoms. For any given electronic configuration, it provides zeroth-order states with quantum numbers (L, S, M_L, κ) and term-specific first-order-corrected energies $E_{LS\kappa}$. On this basis, state-to-state transition parameters for photoionisation, Auger-Meitner decay, and fluorescence are calculated from first principles. Since they are independent of the spin projection M_S, M_S is neglected in this work.

A Monte Carlo on-the-fly rate-equation method[11,12] is employed for describing the time evolution of individual quantum-state populations. The number of individual quantum states involved is already very large for argon[36], i.e., 2^{16}, which would be challenging without a Monte Carlo on-the-fly approach. Next to the Monte Carlo method a couple of simplifications are critical to efficiently perform calculations. We made several approximations: non-sequential two-photon absorption[34,90], higher-order many-body processes such as double photoionisation[91] and double Auger-Meitner decay[92], coherent effects[93–96], inter-channel coupling[97,98], relativistic effects[32,99], finite-nuclear-size effects[99], and non-dipole effects[100,101] are not included in this work.

Due to the Monte Carlo method all presented results contain statistical errors. Statistical errors are obtained via bootstrap estimate[102] using 50 bootstrap samples of 200,000 Monte Carlo trajectories. For the results in Figs. 1 and 2, errors are two orders of magnitude smaller than the dominant quantities themselves and are, consequently, omitted. The calculated errors become quite large, particularly for propagation at early times and for large L in Fig. 3, because the number of ions of interest is too small. To avoid such insufficient statistics, results in Figs. 3 and 4 are only plotted when the underlying ion probability is ≥0.005. We expect that the overall trend shown in Figs. 3 and 4 will remain unchanged when more Monte Carlo trajectories are used.

Data availability
The raw data and the underlying data for the figures can be obtained from the authors upon request.

Code availability
The state-resolved Monte Carlo implementation in the XATOM toolkit is available from the authors upon request.

References

1. Emma, P. et al. First lasing and operation of an ångstrom-wavelength free-electron laser. *Nat. Photon.* **4**, 641–647 (2010).
2. Decking, W. et al. A MHz-repetition-rate hard x-ray free-electron laser driven by a superconducting linear accelerator. *Nat. Photon.* **14**, 391–397 (2020).
3. Kang, H.-S. et al. Hard x-ray free-electron laser with femtosecond-scale timing jitter. *Nat. Photon.* **11**, 708–713 (2017).
4. Ishikawa, T. et al. A compact x-ray free-electron laser emitting in the sub-ångström region. *Nat. Photon.* **6**, 540–544 (2012).
5. Prat, E. et al. A compact and cost-effective hard x-ray free-electron laser driven by a high-brightness and low-energy electron beam. *Nat. Photon.* **14**, 748–756 (2020).
6. Pellegrini, C., Marinelli, A. & Reiche, S. The physics of x-ray free-electron lasers. *Rev. Mod. Phys.* **88**, 015006 (2016).
7. Schulze, K. S. et al. Towards perfectly linearly polarized x-rays. *Phys. Rev. Res.* **4**, 013220 (2022).
8. Allaria, E. et al. Control of the polarization of a vacuum-ultraviolet, high-gain, free-electron laser. *Phys. Rev. X* **4**, 041040 (2014).
9. Santra, R. and Young, L. Interaction of intense x-ray beams with atoms, in *Synchrotron Light Sources and Free-Electron Lasers*, edited by Jaeschke, E. J., Khan, S., Schneider, J. R., and Hastings, J. B. (Springer International Publishing, Switzerland, 2016), pp. 1233–1260. https://doi.org/10.1007/978-3-319-14394-1_25.
10. Young, L. et al. Femtosecond electronic response of atoms to ultra-intense x-rays. *Nature* **466**, 56–61 (2010).
11. Fukuzawa, H. et al. Deep inner-shell multiphoton ionization by intense x-ray free-electron laser pulses. *Phys. Rev. Lett.* **110**, 173005 (2013).
12. Son, S.-K. & Santra, R. Monte Carlo calculation of ion, electron, and photon spectra of xenon atoms in x-ray free-electron laser pulses. *Phys. Rev. A* **85**, 063415 (2012).
13. Rudek, B. et al. Relativistic and resonant effects in the ionization of heavy atoms by ultra-intense hard x-rays. *Nat. Commun.* **9**, 4200 (2018).
14. Rudek, B. et al. Ultra-efficient ionization of heavy atoms by intense x-ray free-electron laser pulses. *Nat. Photon.* **6**, 858–865 (2012).
15. Motomura, K. et al. Sequential multiphoton multiple ionization of atomic argon and xenon irradiated by x-ray free-electron laser pulses from SACLA. *J. Phys. B: Mol. Opt. Phys.* **46**, 164024 (2013).
16. Lorenz, U., Kabachnik, N. M., Weckert, E. & Vartanyants, I. A. Impact of ultrafast electronic damage in single-particle x-ray imaging experiments. *Phys. Rev. E* **86**, 051911 (2012).
17. Quiney, H. M. & Nugent, K. A. Biomolecular imaging and electronic damage using x-ray free-electron lasers. *Nat. Phys.* **7**, 142–146 (2011).
18. Nass, K. Radiation damage in protein crystallography at x-ray free-electron lasers. *Acta Cryst. D.* **75**, 211–218 (2019).
19. Neutze, R., Wouts, R., van der Spoel, D., Weckert, E. & Hajdu, J. Potential for biomolecular imaging with femtosecond x-ray pulses. *Nature* **406**, 752–757 (2000).
20. Son, S.-K., Young, L. & Santra, R. Impact of hollow-atom formation on coherent x-ray scattering at high intensity. *Phys. Rev. A* **83**, 033402 (2011).
21. Spence, J. C. H. XFELs for structure and dynamics in biology. *IUCrJ* **4**, 322–339 (2017).
22. Schlichting, I. & Miao, J. Emerging opportunities in structural biology with x-ray free-electron lasers. *Curr. Opin. Struct. Biol.* **22**, 613–626 (2012).
23. Sobolev, E. et al. Megahertz single-particle imaging at the European XFEL. *Commun. Phys.* **3**, 97 (2020).
24. Seibert, M. M. et al. Single mimivirus particles intercepted and imaged with an x-ray laser. *Nature* **470**, 78–81 (2011).
25. Chapman, H. N. et al. Femtosecond x-ray protein nanocrystallography. *Nature* **470**, 73–77 (2011).
26. Coe, J. & Fromme, P. Serial femtosecond crystallography opens new avenues for structural biology. *Protein Pept. Lett.* **23**, 255–272 (2016).
27. Galli, L. et al. Towards phasing using high x-ray intensity. *IUCrJ* **2**, 627–634 (2015).
28. Nass, K. et al. Structural dynamics in proteins induced by and probed with x-ray free-electron laser pulses. *Nat. Commun.* **11**, 1814 (2020).
29. Chapman, H. N. X-ray free-electron lasers for the structure and dynamics of macromolecules. *Annu. Rev. Biochem.* **88**, 35–58 (2019).
30. Xiang, W., Gao, C., Fu, Y., Zeng, J. & Yuan, J. Inner-shell resonant absorption effects on evolution dynamics of the charge state distribution in a neon atom interacting with ultraintense x-ray pulses. *Phys. Rev. A* **86**, 061401(R) (2012).
31. Rörig, A. et al. Multiple-core-hole resonance spectroscopy with ultraintense x-ray pulses. *Nat. Commun.* **14**, 5738 (2023).
32. Toyota, K., Son, S.-K. & Santra, R. Interplay between relativistic energy corrections and resonant excitations in x-ray multiphoton ionization dynamics of Xe atoms. *Phys. Rev. A* **95**, 043412 (2017).
33. Buth, C. et al. Neon in ultrashort and intense x-rays from free electron lasers. *J. Phys. B: Mol. Opt. Phys.* **51**, 055602 (2018).
34. Doumy, G. et al. Nonlinear atomic response to intense ultrashort x rays. *Phys. Rev. Lett.* **106**, 083002 (2011).
35. Son, S.-K., Boll, R. & Santra, R. Breakdown of frustrated absorption in x-ray sequential multiphoton ionization. *Phys. Rev. Res.* **2**, 023053 (2020).

Article

36. Budewig, L., Son, S.-K. & Santra, R. State-resolved ionization dynamics of a neon atom induced by x-ray free-electron-laser pulses. *Phys. Rev. A* **107**, 013102 (2023).

37. Mazza, T. et al. Mapping resonance structures in transient core-ionized atoms. *Phys. Rev. X* **10**, 041056 (2020).

38. Budewig, L., Son, S.-K. & Santra, R. Theoretical investigation of orbital alignment of x-ray-ionized atoms in exotic electronic configurations. *Phys. Rev. A* **105**, 033111 (2022).

39. Gryzlova, E. V., Grum-Grzhimailo, A. N., Kiselev, M. D. & Popova, M. M. Evolution of the ionic polarization in multiple sequential ionization: general equations and an illustrative example. *Phys. Rev. A* **107**, 013111 (2023).

40. Kleiman, U. & Lohmann, B. Photoionization of closed-shell atoms: Hartree–fock calculations of orientation and alignment. *J. Electron Spectrosc. Relat. Phenom.* **131**-**132**, 29–50 (2003).

41. Caldwell, C. D. & Zare, R. N. Alignment of Cd atoms by photoionization. *Phys. Rev. A* **16**, 255–262 (1977).

42. Southworth, S. H. et al. Photoelectron and Auger electron asymmetries: Alignment of $Xe^{+2}D_{\frac{5}{2}}$ by photoionization. *Phys. Rev. A* **24**, 2257–2260 (1981).

43. Küst, H., Kleiman, U. & Mehlhorn, W. Alignment after Xe L_3 photoionization by synchrotron radiation. *J. Phys. B: Mol. Opt. Phys.* **36**, 2073–2082 (2003).

44. Becker, U. Complete photoionisation experiments. *J. Electron Spectrosc. Relat. Phenom.* **96**, 105–115 (1998).

45. Schmidt, V. Photoionization of atoms using synchrotron radiation. *Rep. Prog. Phys.* **55**, 1483–1659 (1992).

46. Flügge, S., Mehlhorn, W. & Schmidt, V. Angular distribution of Auger electrons following photoionization. *Phys. Rev. Lett.* **29**, 7–9 (1972).

47. Berezhko, E. G., Kabachnik, N. M. & Rostovsky, V. S. Potential-barrier effects in inner-shell photoionisation and their influence on the anisotropy of x-rays and Auger electrons. *J. Phys. B: Mol. Opt. Phys.* **11**, 1749 (1978).

48. Cleff, B. & Mehlhorn, W. On the angular distribution of Auger electrons. *Phys. Lett. A* **37**, 3–4 (1971).

49. Cleff, B. & Mehlhorn, W. Angular distribution of $L_3M_{2,3}M_{2,3}$ ($^1S_0$) Auger electrons of argon. *J. Phys. B: Mol. Opt. Phys.* **7**, 605–611 (1974).

50. Berezhko, E. G. & Kabachnik, N. M. Theoretical study of inner-shell alignment of atoms in electron impact ionisation: angular distribution and polarisation of x-rays and Auger electrons. *J. Phys. B: Mol. Opt. Phys.* **10**, 2467–2477 (1977).

51. Schmoranzer, H. et al. Angular distribution of the fluorescence radiation of Kr II satellite states. *J. Phys. B: Mol. Opt. Phys.* **30**, 4463–4480 (1997).

52. Hrdý, J., Henins, A. & Bearden, J. A. Polarization of the L_{α_1} x rays of mercury. *Phys. Rev. A* **2**, 1708–1711 (1970).

53. Kronast, W., Huster, R. & Mehlhorn, W. Alignment of atoms following photoionisation. *Z. Phys. D.* **2**, 285–296 (1986).

54. Alexei, S. F., Grum-Grzhimailo, N., Gryzlova, E. V. & Kabachnik, N. M. Photoelectron angular distributions and correlations in sequential double and triple atomic ionization by free electron lasers. *J. Mod. Opt.* **63**, 334–357 (2016).

55. Cooper, J. & Zare, R. N. Angular distribution of photoelectrons. *J. Chem. Phys.* **48**, 942–943 (1968).

56. Manson, S. T. & Cooper, J. W. Angular distribution of photoelectrons: Outer shells of noble gases. *Phys. Rev. A* **2**, 2170–2171 (1970).

57. Davis, V. T. *Introduction to Photoelectron Angular Distributions* (Springer, Switzerland, 2022).

58. Al Moussalami, S. et al. First angle-resolved photoelectron measurements following inner-shell resonant excitation in a singly charged ion. *Phys. Rev. Lett.* **76**, 4496–4499 (1996).

59. Rouvellou, B. et al. Photoelectron spectroscopy experiments on singly charged positive-ions using synchrotron radiation. *Nucl. Instrum. Methods Phys. Res., B* **134**, 287–303 (1998).

60. Rouzée, A. et al. Angle-resolved photoelectron spectroscopy of sequential three-photon triple ionization of neon at 90.5 eV photon energy. *Phys. Rev. A* **83**, 031401 (2011).

61. Braune, M. et al. Electron angular distributions of noble gases in sequential two-photon double ionization. *J. Mod. Opt.* **63**, 324–333 (2016).

62. Young, L. et al. X-ray microprobe of orbital alignment in strong-field ionized atoms. *Phys. Rev. Lett.* **97**, 083601 (2006).

63. Santra, R. et al. Strong-field control of x-ray processes, in *Advances in Atomic, Molecular, and Optical Physics*, edited by Arimondo, E., Berman, P. R., and Lin, C. C. (Academic Press, Amsterdam, 2008), vol. 56, pp. 219–257. https://doi.org/10.1016/S1049-250X(08)00014-1.

64. Heinrich-Josties, E., Pabst, S. & Santra, R. Controlling the 2p hole alignment in neon via the 2s-3p fano resonance. *Phys. Rev. A* **89**, 043415 (2014).

65. Mondal, S. et al. Photoelectron angular distributions for the two-photon sequential double ionization of xenon by ultrashort extreme ultraviolet free electron laser pulses. *J. Phys. B: Mol. Opt. Phys.* **46**, 164022 (2013).

66. Ilchen, M. et al. Symmetry breakdown of electron emission in extreme ultraviolet photoionization of argon. *Nat. Commun.* **9**, 4659 (2018).

67. Khubbutdinov, R. et al. High spatial coherence and short pulse duration revealed by the Hanbury Brown and twiss interferometry at the European XFEL. *Struc. Dyn.* **8**, 044305 (2021).

68. Ferguson, K. R. et al. The atomic, molecular and optical science instrument at the linac coherent light source. *J. Synchrotron Rad.* **22**, 492–497 (2015).

69. Tschentscher, T. et al. Photon beam transport and scientific instruments at the European XFEL. *Appl. Sci.* **7**, 592 (2017).

70. Mazza, T. et al. The beam transport system for the small quantum systems instrument at the European XFEL: optical layout and first commissioning results. *J. Synchrotron Rad.* **30**, 457–467 (2023).

71. Rudenko, A. et al. Femtosecond response of polyatomic molecules to ultra-intense hard x-rays. *Nature* **546**, 129–132 (2017).

72. Murphy, B. F. et al. Femtosecond x-ray-induced explosion of C_{60} at extreme intensity. *Nat. Commun.* **5**, 4281 (2014).

73. Blum, K. *Density Matrix Theory and Applications* (Springer, New York, 1996).

74. Greene, C. H. & Zare, R. N. Photofragment Alignment and Orientation. *Ann. Rev. Phys. Chem.* **33**, 119–150 (1982).

75. Toyota, K. et al. xcalib: a focal spot calibrator for intense x-ray free-electron laser pulses based on the charge state distributions of light atoms. *J. Synchrotron Rad.* **26**, 1017–1030 (2019).

76. Ueda, K. et al. Angular distribution of Auger electrons in resonantly enhanced transitions from 3p photoexcited Ca^+ ions. *J. Phys. B: Mol. Opt. Phys.* **31**, 4331–4348 (1998).

77. Lohmann, B. *Angle and Spin Resolved Auger Emission* (Springer, Berlin Heidelberg, 1994).

78. Lohmann, B. Analyses and model calculations on the angular distribution and spin polarization of Auger electrons. *J. Phys. B: Mol. Opt. Phys.* **23**, 3147–3166 (1990).

79. Blum, K., Lohmann, B. & Taute, E. Angular distribution and polarisation of Auger electrons. *J. Phys. B: Mol. Opt. Phys.* **19**, 3815–3826 (1986).

80. Albiez, A., Thoma, M., Weber, W. & Mehlhorn, W. $KL_{2,3}$ ionization in neon by electron impact in the range 1.5-50 keV: cross sections and alignment. *Z. Phys. D.* **16**, 97–106 (1990).

81. Krässig, B. et al. Nondipolar asymmetries of photoelectron angular distributions. *Phys. Rev. Lett.* **75**, 4736–4739 (1995).

82. Chen, M. H. Effect of intermediate coupling on angular distribution of Auger electrons. *Phys. Rev. A* **45**, 1684–1689 (1992).

83. Mazza, T. et al. Determining the polarization state of an extreme ultraviolet free-electron laser beam using atomic circular dichroism. *Nat. Commun.* **5**, 3648 (2014).

84. Lutman, A. A. et al. Polarization control in an x-ray free-electron laser. *Nat. Photon.* **10**, 468–472 (2016).

85. Prat, E. et al. An x-ray free-electron laser with a highly configurable undulator and integrated chicanes for tailored pulse properties. *Nat. Commun.* **14**, 5069 (2023).

86. Perosa, G. et al. Femtosecond polarization shaping of free-electron laser pulses. *Phys. Rev. Lett.* **131**, 045001 (2023).

87. Jurek, Z., Son, S.-K., Ziaja, B. & Santra, R. XMDYN and XATOM: versatile simulation tools for quantitative modeling of x-ray free-electron laser induced dynamics of matter. *J. Appl. Cryst.* **49**, 1048–1056 (2016).

88. Son, S.-K. et al. XATOM—an integrated toolkit for x-ray and atomic physics, in XRAYPAC, v2.0.0 (2024), GitLab https://gitlab.desy.de/CDT/xraypac.

89. Rudek, B. et al. Resonance-enhanced multiple ionization of krypton at an x-ray free-electron laser. *Phys. Rev. A* **87**, 023413 (2013).

90. Sytcheva, A., Pabst, S., Son, S.-K. & Santra, R. Enhanced nonlinear response of Ne^{8+} to intense ultrafast x rays. *Phys. Rev. A* **85**, 023414 (2012).

91. Schneider, T., Chocian, P. L. & Rost, J.-M. Separation and identification of dominant mechanisms in double photoionization. *Phys. Rev. Lett.* **89**, 073002 (2002).

92. Kolorenč, P., Averbukh, V., Feifel, R. & Eland, J. Collective relaxation processes in atoms, molecules and clusters. *J. Phys. B: Mol. Opt. Phys.* **49**, 082001 (2016).

93. Rohringer, N. & Santra, R. X-ray nonlinear optical processes using a self-amplified spontaneous emission free-electron laser. *Phys. Rev. A* **76**, 033416 (2007).

94. Rohringer, N. & Santra, R. Resonant Auger effect at high x-ray intensity. *Phys. Rev. A* **77**, 053404 (2008).

95. Kanter, E. P. et al. Unveiling and driving hidden resonances with high-fluence, high-intensity x-ray pulses. *Phys. Rev. Lett.* **107**, 233001 (2011).

96. Li, Y. et al. Coherence and resonance effects in the ultra-intense laser-induced ultrafast response of complex atoms. *Sci. Rep.* **6**, 18529 (2016).

97. Drake, G. W. F. *Springer Handbook of Atomic, Molecular, and Optical Physics* (Springer, New York, 2006).

98. Starace, A. F. Trends in the theory of atomic photoionization. *Appl. Opt.* **19**, 4051–4062 (1980).

99. Deslattes, R. D. et al. X-ray transition energies: new approach to a comprehensive evaluation. *Rev. Mod. Phys.* **75**, 35–99 (2003).

100. Demekhin, P. V. On the breakdown of the electric dipole approximation for hard x-ray photoionization cross sections. *J. Phys. B: Mol. Opt. Phys.* **47**, 025602 (2014).

101. Hemmers, O., Guillemin, R. & Lindle, D. W. Nondipole effects in soft X-ray photoemission. *Radiat. Phys. Chem.* **70**, 123–147 (2004).

102. Efron, B. & Tibshirani, R. J. *An introduction to the bootstrap* (Chapman and Hall/CRC, Philadelphia, PA, 1994).

Acknowledgements

Author contributions

L.B. carried out the calculations using the XATOM toolkit, interpreted the results and wrote the manuscript with input from all authors. S.-K.S. and R.S. jointly supervised this work.

Funding

Competing interests

The authors declare no competing interests.

Additional information

Correspondence and requests for materials should be addressed to Robin Santra.

Peer review information *Communications Physics* thanks the anonymous reviewers for their contribution to the peer review of this work.

Reprints and permissions information is available at http://www.nature.com/reprints

Publisher's note Springer Nature remains neutral with regard to jurisdictional claims in published maps and institutional affiliations.